JGR Space Physics

RESEARCH ARTICLE
10.1029/2019JA027551

Tomographic Imaging of Traveling Ionospheric Disturbances Using GNSS and Geostationary Satellite Observations

Karl Bolmgren[1], **Cathryn Mitchell**[1], **Jon Bruno**[1], **and Gary Bust**[2]

[1]Department of Electronic and Electrical Engineering, University of Bath, Bath, UK, [2]Johns Hopkins University Applied Physics Laboratory, Laurel, MD, USA

Key Points:
- Ionospheric tomography with GEO geometry is tested by simulation
- Using GEO geometry improves tomographic imaging of MSTIDs
- Regular GNSS-MEO geometry or a combination of GEO and GNSS-MEO geometry is preferred for LSTIDs

Correspondence to:
K. Bolmgren,
k.h.a.bolmgren@bath.ac.uk

Citation:
Bolmgren, K., Mitchell, C., Bruno, J., & Bust, G. S. (2020). Tomographic imaging of traveling ionospheric disturbances using GNSS and geostationary satellite observations. *Journal of Geophysical Research: Space Physics*, *125*, e2019JA027551. https://doi.org/10.1029/2019JA027551

Received 17 OCT 2019
Accepted 11 FEB 2020
Accepted article online 19 FEB 2020

Abstract Traveling ionospheric disturbances (TIDs) are the manifestations of atmospheric gravity waves in the ionosphere. These disturbances have practical importance because they affect satellite navigation technologies such as Global Navigational Satellite System (GNSS), causing degradation in precise positioning applications. They also have scientific significance as their generation mechanisms and propagation are not fully understood. While there are specific instruments that can measure TIDs in certain locations, there is a need for wide-area observations across extended geographical regions to continuously monitor their onset and spatial and temporal characteristics. This paper evaluates the use of observations from ground-based geodetic GNSS receivers to image TIDs using ionospheric tomography and data assimilation. Certain GNSS receivers also monitor signals from geostationary (GEO) satellites, which provide a unique perspective on the TID. The advantage of using the GEO data is investigated. A computerized simulation of GNSS observations is used for evaluation of the Multi-Instrument Data Analysis System (MIDAS) with GEO and regular GNSS geometry. The simulated observations are generated by integrating the electron density through a modeled TID-perturbed dynamic ionosphere between actual receiver and satellite positions. The output 3-D electron density image series generated from the synthetic data by the MIDAS ionospheric tomography and data assimilation algorithm are compared with the input model ionosphere. Results show that GEO geometry improves the reconstruction of medium-scale TIDs (MSTIDs) and smaller LSTIDs in cases where the movement of regular GNSS satellites in Medium Earth orbit (MEO) may otherwise introduce distortions to the observations.

1. Introduction

The ionosphere, the ionized region of the upper atmosphere, has a significant effect on radio signals at frequencies up to several GHz. Radio transmissions are delayed and refracted when they encounter the electrically charged ionospheric plasma. This makes understanding the spatial and temporal distribution of the ionosphere important for radio communications.

Perturbations in the ionospheric electron density can have a significant impact on precise positioning algorithms using Global Navigational Satellite Systems (GNSS) (Hernández-Pajares et al., 2006a, 2006b). Travelng ionospheric disturbances (TIDs) are a common type of ionospheric disturbance present at most latitudes. TIDs are the ionospheric signatures of atmospheric gravity waves (AGWs) and manifest as propagating wave-like perturbations in ionospheric plasma density, velocity, and temperature. The changes in plasma density are important for radio propagation. The amplitude, period, and spatial wavelength of TIDs vary, and they are typically categorized as either medium scale or large scale. Medium-scale TIDs (MSTIDs) have periods below 1 hr and horizontal wavelengths between 100 and 1,000 km, while large-scale TIDs (LSTIDs) have typical periods between 0.5 and 3 hr, and wavelengths above 1,000 km (Hocke & Schlegel, 1996). TIDs can be initiated by processes in the troposphere as well as the ionosphere. An important source of MSTIDs is the solar terminator (Hernández-Pajares et al., 2006b; Nygrén et al., 2015). LSTIDs, on the other hand, are commonly associated with geomagnetically perturbed conditions and tend to travel equatorward from auroral latitudes (Davis & da Rosa, 1969). Although TIDs have been investigated for many years, interesting outstanding questions remain about the source mechanisms and it is still not possible to include them in ionospheric forecasting models.

TIDs have been observed by various ionospheric instruments. The first observations of TIDs were made by ionosondes in Australia and were described by Munro (1950). Other commonly used instruments for

TID observation include incoherent scatter radars, airglow imagers, and dual frequency GNSS receivers. GNSS receiver networks, in particular, are important tools for studying TIDs over large spatial scales. Several studies have produced 2-D maps of TID-induced perturbations in vertical total electron content (vTEC) over such networks, as was first done by Saito et al. (1998). However, GNSS observations of TIDs are subject to distortion due to the movement of the satellites relative to the TID, which must be taken into account in many cases (Hernández-Pajares et al., 2006b; Penney & Jackson-Booth, 2015; Van De Kamp et al., 2014; Wan et al., 1997).

Each of these instruments has difficulty capturing the full spatial characteristics of TIDs without additional information. For example, Van De Kamp et al. (2014) used incoherent scatter radar observations to provide vertical information in order to complement the horizontal information provided by GPS observations. Incoherent scatter radars are, however, only available in a few locations worldwide, and in areas without complementing instruments like these it is still possible to infer horizontal information by using radio tomography methods.

Ionospheric radio tomography, introduced by Austen et al. (1988), is a method used to image the ionospheric free electron number density $N(\mathbf{x}, t)$ distribution in 2-D, 3-D, or 4-D using sets of total electron content (TEC) data. TEC measured using GNSS is the electron density integrated along the ray path C_{ij} between satellite i and receiver j at time t,

$$TEC_{ij}(t) = \int_{C_{ij}} N(\mathbf{x}, t)\ \mathrm{d}l, \tag{1}$$

and is inferred from the phase advance and code delay observed by the receiver in the radio signals transmitted from the GNSS satellite.

Methods for ionospheric tomography were initially developed for low earth orbiting satellites such as those part of the Cicada and Transit constellations. These methods were successful in imaging MSTIDs along strings of ground receivers thanks to the fast low earth orbiting satellite passes (Cook & Close, 1995; Kunitake et al., 1995; Pryse et al., 1995). Increasing GNSS ground receiver coverage has since shifted focus toward GNSS satellites in medium earth orbit (MEO). A review of ionospheric tomography can be found in Bust and Mitchell (2008). GNSS tomography has also been applied in efforts to observe TIDs (as evidenced in Chen et al., 2016; Lee et al., 2008; Ssessanga et al., 2015; Tang et al., 2016; Yin et al., 2017; Yizengaw et al., 2005).

The movement of a GNSS satellite over a time period introduces a movement of the ray between satellite and receiver, and thus the integration path through the ionosphere C_{ij} in equation (1). The movement of an ionospheric pierce point (IPP), a point where the ray intersects the ionosphere at a specified height, may reach velocities close to those of the TIDs themselves, which introduces distortions in the wave parameters observed in the TEC time series (Penney & Jackson-Booth, 2015; Van De Kamp et al., 2014; Wan et al., 1997).

A way to avoid these distortions is to eliminate the relative movement of satellite-receiver ray and TID by using observations from satellites in Geostationary Orbit (GEO). Ground observations of Faraday rotation of signals sent from satellites in GEO have previously been used to study TIDs (e.g., Davis & da Rosa, 1969). The advantage of using GEO has been recognized by recent work: for example, Huang et al. (2018) who compared observations of nighttime MSTIDs from GPS TEC, Beidou GEO TEC, and airglow observations over central China. They concluded that although the different observations generally agreed, GEO TEC and airglow were in closest agreement. They attributed this to distortion effects from GPS satellite movement.

In areas such as Europe and North America, which are outside the coverage of Beidou satellites in GEO, satellites in the Satellite Based Augmentation System (SBAS) constellations WAAS and EGNOS may be used instead. Kunitsyn et al. (2016) showed that the use of SBAS GNSS signals leads to a significantly higher TEC error when compared to signals from Beidou satellites in GEO. However, Cooper et al. (2019) recently introduced a new method to calculate relative TEC from SBAS single frequency signals broadcast from GEO, improving the viability of using GEO TEC with ionospheric tomography in areas covered by SBAS. In summary, there are a number of GEO signals available that could be used in ionospheric tomography and have the potential to improve the resulting images in a range of geographical regions.

This simulation study examines the possible improvement in TID imaging from the addition of GEO TEC observations to the Multi-Instrument Data Analysis System (MIDAS) tomographic algorithm (Mitchell & Spencer, 2003). The simulation approach is outlined in Figure 1. The main steps are described in section 2. In section 2.1 an ionospheric electron density model is constructed as the ground truth. Section 2.2 explains

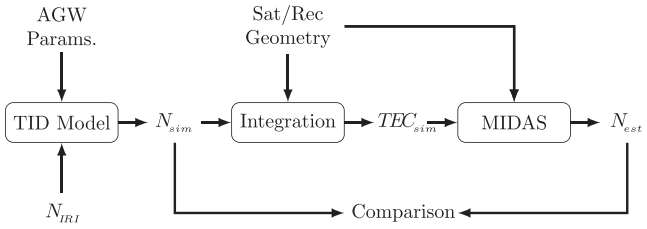

Figure 1. Flowchart of the method validation procedure. The Hooke TID model uses both AGW parameters and an IRI background N_{IRI} to produce the simulated test ionosphere N_{sim}. Receiver and satellite (GEO, GNSS-MEO, or both) geometries are added first to integrate through N_{sim} to produce the synthetic TEC data TEC_{sim}, and then to the MIDAS algorithm for the reconstruction. Finally, the output N_{est} is compared to the input N_{sim}.

how the model is used to generate synthetic TEC observations from satellites in GEO and GNSS satellites in MEO. These are used by the MIDAS algorithm, described and referenced in section 2.3, to reconstruct the 4-D electron density spatial and temporal distribution. In section 3 the MIDAS inversion results are compared to the modeled electron density in order to evaluate the inversion method and examine the effects of using observations from different satellite orbits to provide TEC.

2. Method

2.1. TID Model

A modeled ionosphere is used to evaluate the MIDAS algorithm for TID imaging by providing test data and a ground truth. The first part of the model is the unperturbed electron density, or background. This background is generated using the International Reference Ionosphere 2016 (IRI) (Bilitza et al., 2017). The TID-induced modulation of the background is calculated from AGW parameters using the physics-based Hooke (1968) model. In this model the electron density is given by

$$N_{\mathrm{sim}}(\mathbf{x},t) = N_0(\mathbf{x},t) + \delta N(\mathbf{x},t), \tag{2}$$

where the perturbation δN is given by

$$\delta N = N_0 \frac{U_b \sin I}{\omega} e^{k_{zi}(z-z_0)} \left[\left(\frac{\partial_z N_0}{N_0} + k_{zi} \right)^2 + \frac{k_{\mathrm{br}}^2}{\sin^2 I} \right]^{1/2} \cdot \cdot \cos \left[\omega t - \mathbf{k}_r \cdot \mathbf{x} - \tan^{-1} \left(\frac{k_{\mathrm{br}}/\sin I}{\partial_z N_0/N_0 + k_{zi}} \right) \right] \tag{3}$$

where $\partial_z N_0$ is the vertical density gradient of the background, U_b is the neutral velocity in the direction parallel to the geomagnetic field at a reference height z_0, ω is the angular AGW frequency, I is the geomagnetic inclination, k_{br} is the real part of the wave vector $\mathbf{k}$ parallel to the geomagnetic field and k_{zi} is the imaginary part of $\mathbf{k}$, which is only nonzero in the vertical direction. The values for the geomagnetic field are taken from the International Geomagnetic Reference Field (Thébault et al., 2015).

This type of model has been implemented to model TIDs in several recent studies (Cervera & Harris, 2014; Mitchell et al., 2017; Nickisch et al., 2016), and the model itself was tested by Morgan and Calderón (1978) who found relatively good agreement with measurements. The main drawbacks of this model is that there is no viscosity effect to damp out the wave at higher altitudes, and that the scale height is constant with altitude.

Here, following Hooke (1968), the assumption is made that there is no dissipation in order to get a simple estimate of the imaginary part of wave vector ($k_{zi} = 1/2H$). The horizontal and vertical wavelengths are related to each other and the angular frequency ω by the AGW dispersion relation (Hines, 1960)

$$k_z = k_h \left(\frac{\omega_B^2}{\omega^2} - 1 \right) + \frac{\omega^2 - \omega_a^2}{c^2}, \tag{4}$$

where $\omega_B = (\gamma - 1)g/(\gamma H)$ is the Brunt-Väisälä frequency and $\omega_a = c/2H$ is the acoustic cutoff frequency. In these expressions, c is the speed of sound and γ the specific heat ratio. For simplicity, constant values $H = 50$ km, $\gamma = 1.4$ and $c = \sqrt{\gamma g H} = 829$ m/s are used.

The model equation (3) was derived using a linearized perturbation treatment, and the physical approximations are valid only in the bottomside ionospheric F region. An additional exponential dampening is therefore applied above the $F2$ peak and below the upper $F1$ region when calculating the perturbation field $\delta N(\mathbf{x}, t)$. This approach may lead to an unrealistic response of the top-side ionosphere, where the effects of the TID are diminished.

2.2. Simulated TEC Observations

The ionosphere simulation outlined in Figure 1 uses synthetic TEC observations TEC_{sim} generated from six different simulated ionospheric electron density structures $N_{\mathrm{sim}}(\mathbf{x}, t)$. These model ionospheres are constructed as described in section 2.1, and only differ by AGW/TID parameter inputs to equation (3), which

Table 1
TID Wave Parameters Used to Generate the Six Test Ionospheres N_{sim}

TID no.	1	2	3	4	5	6
T (min)	90	75	60	45	30	20
λ (km)	3,000	2,000	1,500	1,000	500	300

Note. $T = 2\pi/\omega$ is the wave period and $\lambda = 2\pi/k_h$ is the horizontal wavelength. All TIDs are directed north-south.

are listed in Table 1. The background ionospheres were generated with IRI every 5 min, and interpolated linearly in time every 30 s, between 6 and 18 UT for 27 September 2016, a time with moderate geomagnetic conditions (Kp between 4 and 6) toward the end of the 24th solar cycle (monthly smoothed sunspot number of 33.2). The simulated TEC observations are integrated along each satellite-receiver ray path every 30 s according to equation (1), with N equal to the modeled electron density, N_{sim}.

The 30-s interval is chosen as this is the usual rate at which GNSS data are collected and stored on ground-based geodetic receivers. It is assumed that the bending of the ray path due to refraction is negligible, which simplifies the ray paths to straight lines between satellites and receivers. The coordinates of 191 receiver stations belonging to the International GNSS Service (IGS) and UNAVCO networks in North America, and real GPS and GLONASS precise satellite orbits provided by IGS are used to provide the geometry for the synthetic TEC observations. The positions of three satellites in the WAAS SBAS constellation: Inmarsat 4-F3 (98°W, PRN 133), Intelsat Galaxy 15 (133°W, PRN 135) and TeleSat Anik F1R (107.3°W, PRN 138) represent the geostationary satellite geometry. Any observation with elevation below 10° is discarded from the simulated synthetic observations. No inter-frequency biases (IFBs) are added to the synthetic observations, as they have no effect on the regular MIDAS inversion (Bruno et al., 2020; Dear & Mitchell, 2006).

2.3. MIDAS Tomography Algorithm

The tomography method used in this study is the University of Bath MIDAS time-dependent inversion algorithm. In the ionospheric mode, MIDAS can take in any observation that is related to electron density. The standard mode for MIDAS to use GNSS is to take in dual frequency carrier-phase measurements to image the time-varying ionospheric free electron distribution in three spatial dimensions. For these inversions empirical orthogonal functions (EOFs) seeded with a set of Chapman functions (Chapman, 1931) provide the vertical electron density structure and reduce the complexity of the inverse problem. TEC observations, sampled from a time window weighted centrally around the current inversion time step, are

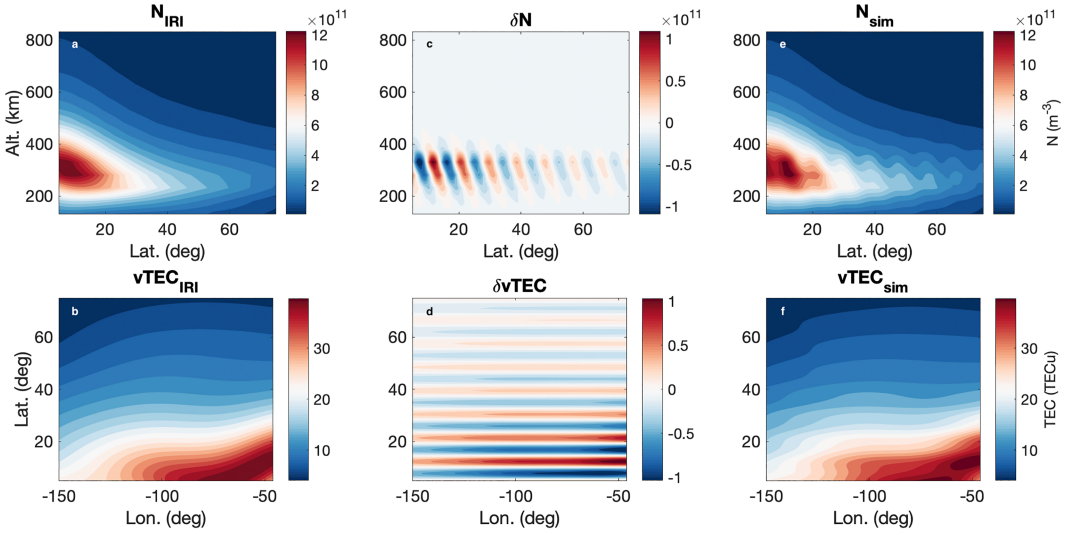

Figure 2. Panels (a) and (b) show the background model ionosphere N_{IRI} as a cross section at 98°W and as vertical TEC, respectively. Panels (c) and (d) show the modeled perturbation δN as generated by using equation (3) with $N_0 = N_{\text{IRI}}$ and wave parameters corresponding to TID 4 in Table 1. When added, the background and perturbation form the simulated electron density N_{sim} shown in panels (e) and (f).

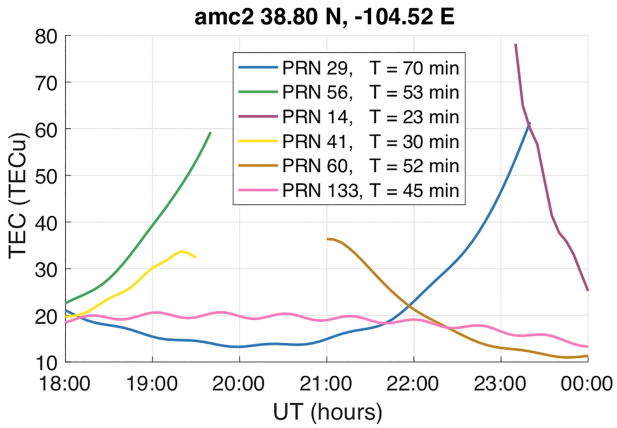

Figure 3. Simulated TEC measurements (TEC_{sim}) generated from a southward Traveling TID (TID 4) with period 45 min and horizontal wavelength 1,000 km for five selected GNSS-MEO satellites and one geostationary satellite (PRN 133) as seen from receiver amc2 (38.8°N, 104.5°W). The apparent periods T vary with the direction of satellite movement, shown in Figure 4.

used for the inversion. MIDAS can use either uncalibrated TEC that is ray-differenced for the inversion, as first done by Andreeva et al. (1992), or precalibrated TEC observations that have been corrected for biases. Ray-differenced TEC means the difference between consecutive 30-s TEC samples over the same satellite-receiver link. When precalibrated measurements are used, they must first be corrected for IFBs in both satellites and receivers. However, the calibration of IFBs can be problematic for real-time operations and hence MIDAS usually inputs only phase observations. The ray-differencing procedure is integrated into MIDAS, so the same data set can be used with either setting.

For this study 3-D images of the electron density are reconstructed at 5-min intervals. The data time window is 1 hr wide and the voxels for the model and inversion are 25 km by 0.5° by 2° in height, latitude, and longitude, respectively. The latitude-longitude grid is set to balance the capability to resolve TIDs while not creating too many unknowns to solve in the inverse problem. The data time window of 1 hr was selected to provide enough data to be able to solve the inverse problem with this relatively high latitudinal resolution. This presents a trade-off between the size of the time window and the spatial resolution. A large time window lets more data be used for each inversion, but can cause other problems when the movement of the satellite and TID are involved. The height resolution is only used to map between the EOF representation of the

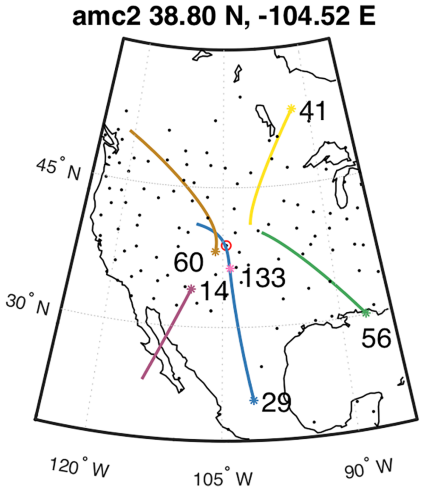

Figure 4. Tracks of satellite IPPs, at a height of 300 km, corresponding to the TEC time series in Figure 3. The last satellite positions as seen from the receiver are indicated by asterisks. The IPP of PRN 133 is shown only as an asterisk, as it appears stationary relative to the surface of the Earth. Black dots represent locations of receivers used in the inversion, and the location of amc2 is indicated by a circled dot.

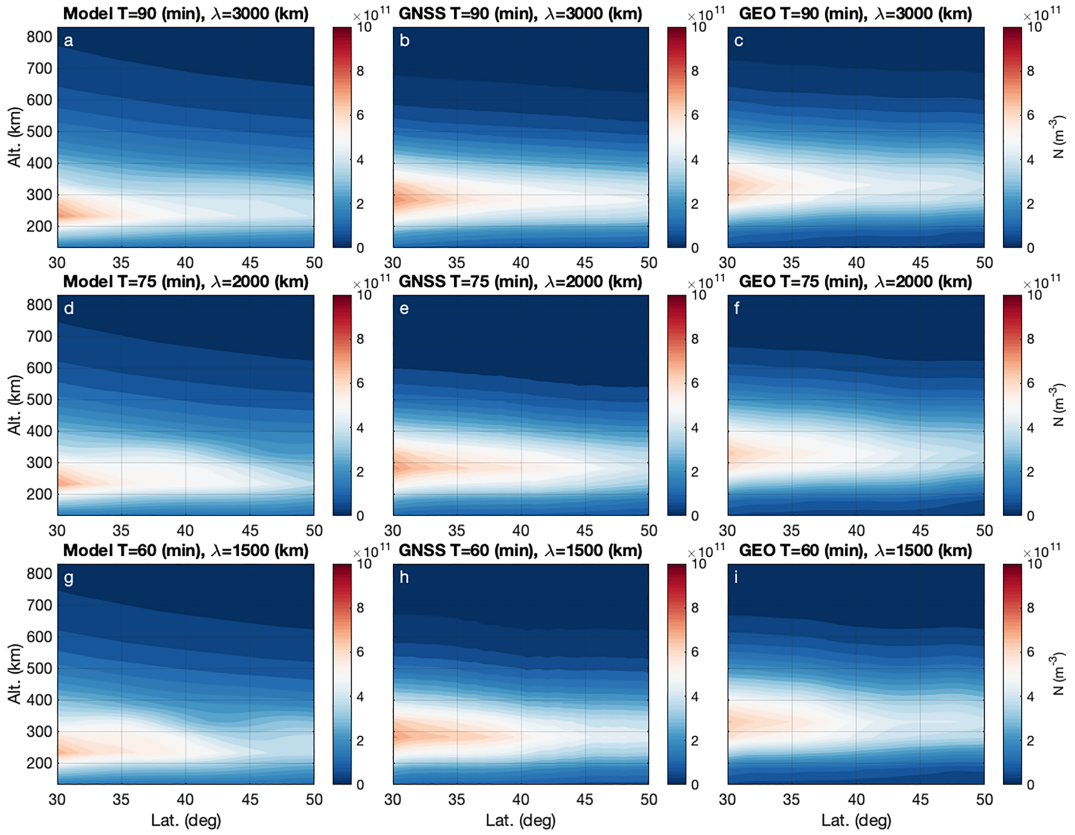

Figure 5. Modeled electron density N_{sim} (a, d, and g) and inversion results N_{est} (m^{-3}) (b, c, e, f, h, and i) for TIDs 1–3 when treating the input data as precalibrated, that is, without ray differencing. Panels (b), (e), and (h) show GNSS-MEO results, and panels (c), (f), and (i) show GEO-only results.

height distribution and the voxel representation. This means that the height resolution can be chosen freely without affecting the number of unknowns in the inverse problem.

3. Results

Simulated line-integrated TEC observations were generated for the six different modeled TIDs in Table 1, generated as described in section 2.2, with two types of geometry: one using only GPS and GLONASS satellites in MEO, and a second using three satellites in GEO. It is important to stress here that the models are dynamic—they represent a propagating TID, and each integration to produce TEC is at the relevant time in the TID's movement. This is to make the simulated observations as realistic as possible. These TEC observations were then inverted using MIDAS to produce electron density structures $N_{est}(\mathbf{x}, t)$ for GEO satellite geometry, GNSS-MEO satellite geometry and a combined geometry and each of these for calibrated TEC and ray-differenced TEC input.

3.1. Modeling Results

The modeling procedure described in section 2.1 was used to generate six TID-perturbed ionospheric electron density structures, N_{sim}, over North America. Figure 2 shows an example, with AGW/TID parameters from TID 4 in Table 1, of the two parts (Figures 2a and 2b) and the perturbation (Figures 2c and 2d). The full structure with background and TID combined is given in (Figures 2e and 2f). The three top plots show slices through the three-dimensional electron density structures, and the bottom plots show the same models integrated vertically to obtain vTEC.

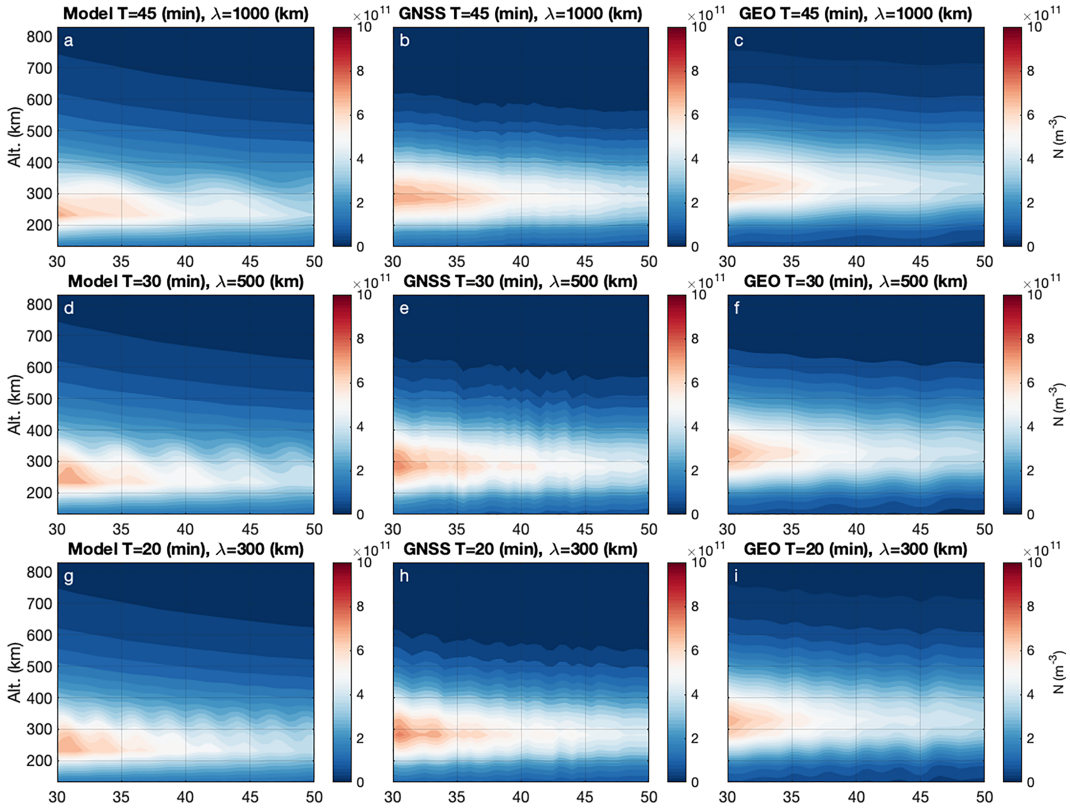

Figure 6. Modeled electron density N_{sim} (a, d, and g) and inversion results N_{est} (m^{-3}) (b, c, e, f, h, and i) for TIDs 4–6 when treating the input data as precalibrated, that is, without ray differencing. Panels (b), (e), and (h) show GNSS-MEO results, and panels (c), (f), and (i) show GEO-only results.

3.2. Synthetic Data Results

TEC data were simulated for each model ionosphere, and all satellite geometries. Examples of simulated TEC observations from one receiver and six selected satellites (from a time-dependent ionosphere, a single frame from which is shown in Figure 2) are plotted in Figure 3 together with estimated wave periods T. Caution should be exercised here as the apparent wave periods when interpreted from this graph are dependent on the direction of movement of the satellite relative to the TID direction of travel. This can be viewed alongside Figure 4 which shows IPP tracks at an altitude of 300 km. This altitude was chosen to coincide with the height where the modeled TID affects the largest effect on the ionosphere. For example, the satellite identified by pseudo-random-noise code (PRN) 41 moves against the TID propagation direction and shows an apparent wave period shorter than in the simulation. PRN 60, on the other hand, moving more in the TID direction, displays a larger apparent period. The geostationary PRN 133 TEC_{sim} TEC series most closely reproduces the simulated TID period (45 min). It is clear from these examples that satellite movement can have a large impact on the apparent wave periods of the TEC. This shows that the observations themselves can exhibit distortion of the actual wave parameters.

3.3. Inversion Results Using Precalibrated TEC

The first stage of evaluating the inversions is now to determine the difference between the simulated ionosphere and the MIDAS tomography electron density output when treating the synthetic TEC observations as "perfect" (i.e., precalibrated) TEC input data. This means that no ray differencing of the TEC is performed as part of the inversion. The MIDAS inversion results using GNSS-MEO and GEO geometry for the TIDs in Table 1 are shown in Figures 5 and 6 as electron density cross-section snapshots in height and latitude. The modeled wave perturbations are especially clear in the GEO inversion and less evident in the GNSS results, where the waves are somewhat obscured by smaller artifacts. However, examination of the vTEC sampled at one point in the middle of the reconstruction grid, as plotted in Figure 7 reveals that the modeled TIDs are also present in the GNSS inversion.

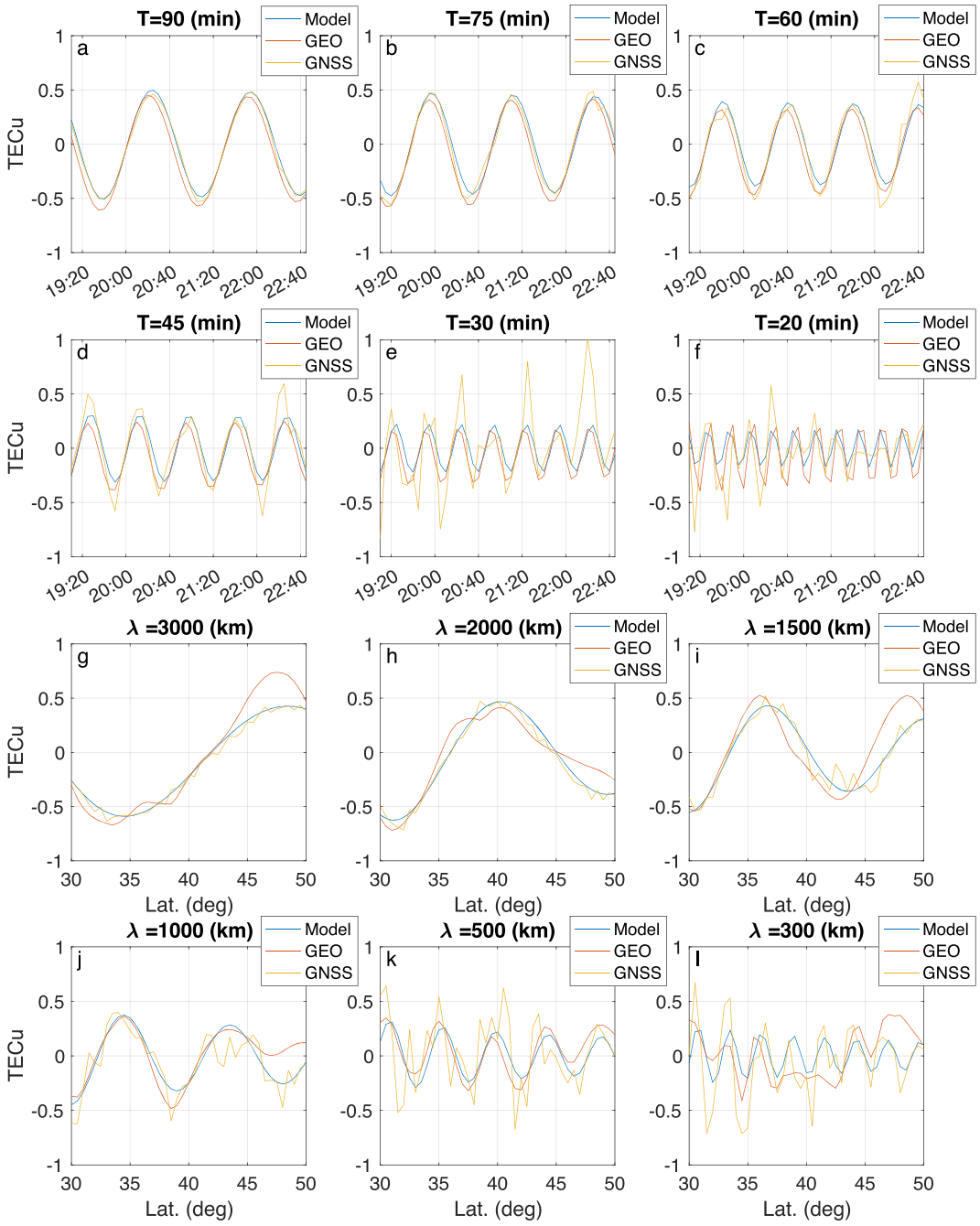

Figure 7. Precalibrated TEC inversion results ($vTEC_{\text{est}}^{\text{GNSS-MEO}} - vTEC_0$) and ($vTEC_{\text{est}}^{\text{GEO}} - vTEC_0$) plotted against the model δTEC.

In Figure 7 the modeled perturbations δN and the difference between the reconstruction and the modeled background ($N_{\text{est}} - N_0$) are compared in order to get a clearer view of the wave-like behavior. Figures 7a–7f show the sampled vTEC as time series, and Figures 7g–7l show vTEC for all latitudes at one time step. Figures 7d–7f and 7j–7l illustrate how the GNSS inversion has trouble with smaller TIDs, while the GEO inversion vTEC is reasonably accurate for all but the smallest modeled TID (Figures 7f and 7l). It should also be noted that the background N_0 would not be known a priori in a real data scenario and must be estimated by image filtering.

Some spatial artifacts smaller than the modeled TIDs appear in all GNSS inversions, as evident in Figure 7. For TIDs 1–2 they appear as small variations below 0.1 TECu in amplitude around an otherwise well

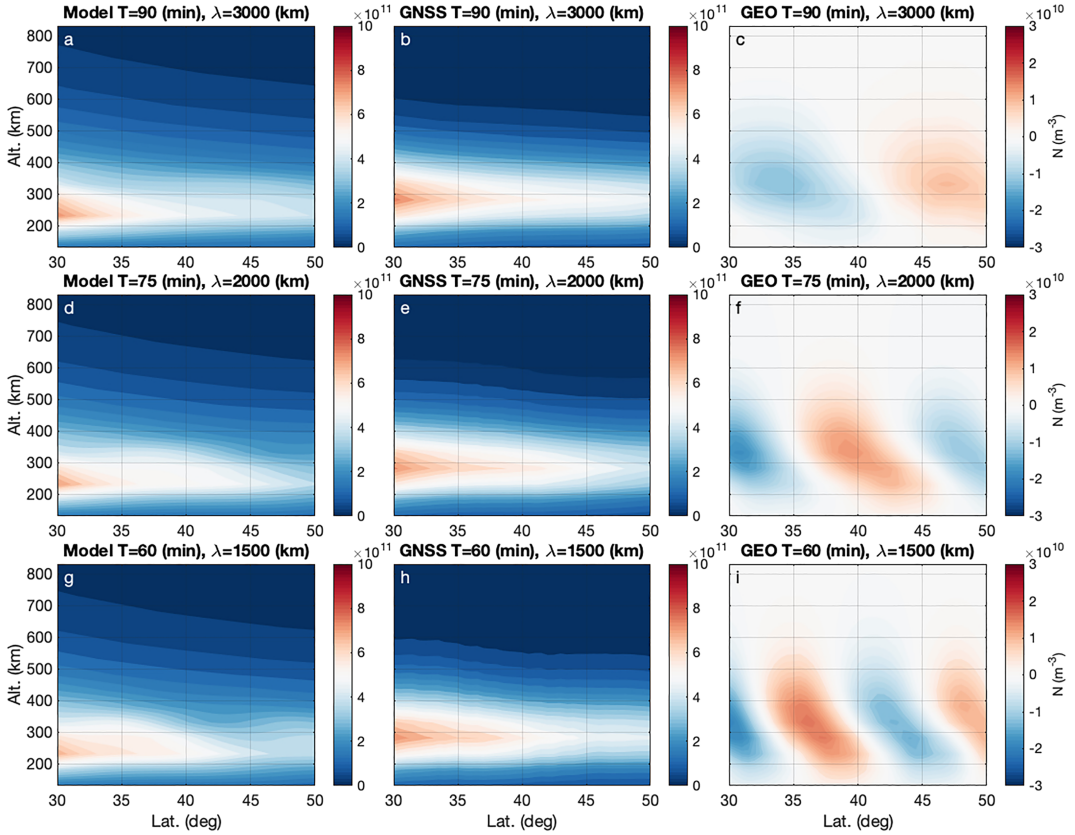

Figure 8. Modeled N_{sim} and inversion results N_{est} (m^{-1}) for TIDs 4–6 using ray-differenced TEC. Panels (b), (e), and (h) show GNSS-MEO results, andpanels (c), (f), and (i) show GEO results.

estimated vTEC. They are more apparent for TIDs 3–6 in Figures 7i–7l, where the artifacts reach amplitudes around 0.2 TECu. It is interesting that the GNSS reconstructions tend to overshoot the TID wave amplitudes for the smallest TIDs by as much as approximately 5 times the amplitude, as is the case for one wave crest in Figure 7e.

3.4. Inversion Results Using Ray-Differenced TEC

If no reliable IFB estimates are available, the MIDAS algorithm can run in a ray-difference mode, where the inversion algorithm inverts for changes in electron density rather than absolute values.

For slowly changing electron density N_{sim} the simulated ray-differenced TEC values become very small when using GEO satellite geometry, which makes this inversion configuration less sensitive to slow, large-scale changes like those present in IRI. This means that GEO with MIDAS in ray-difference mode is much more sensitive to the sharp density gradients in the perturbation δN caused by the modeled TIDs than to the background N_0. This sometimes gives us a clear view of the modeled TIDs as displayed in Figure 8, which shows the TEC inversion results for TIDs 4–6. For the larger TIDs 1–3 in Figure 9, the structures are faint compared to the modeled density perturbations. This effect is also seen in the vTEC of Figure 10, where larger TIDs yield underestimated amplitudes when using GEO geometry.

The results from the ray-differenced GNSS-MEO inversions are similar to the absolute inversions, apart from a small shift in overall background vTEC for some of the inversions. These arise from the need to calibrate the absolute values within the reconstruction algorithm. The artifacts seen in the precalibrated results are equally apparent in Figures 10e and 10f and 10j–10l (TIDs 4–6), and the amplitudes are again occasionally overestimated when using GNSS.

3.5. Comparing GEO-Only and GNSS-MEO Results

When using calibrated TEC, both GEO and GNSS-MEO data produce inversions with TIDs clearly visible for all but the smallest TID. The largest error in vTEC between the model and the GEO reconstruction is around 0.25 TECu, after the modeled background N_0 has been removed.

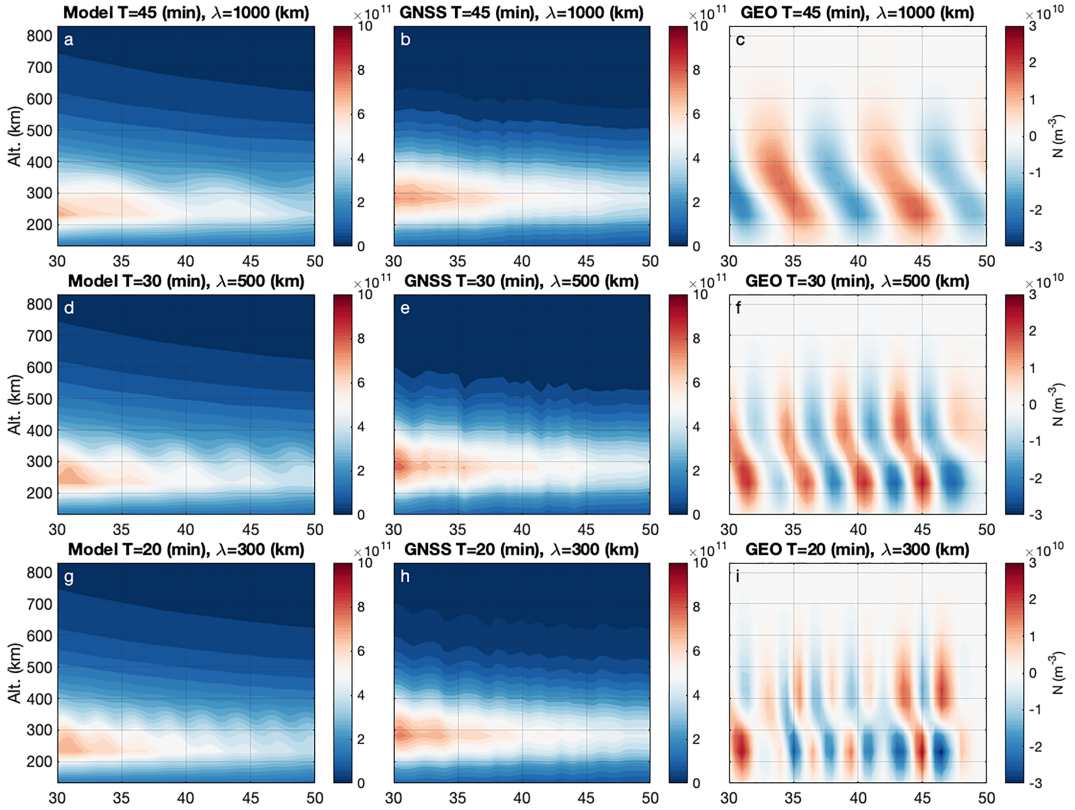

Figure 9. Modeled N_{sim} and inversion results N_{est} (m^{-1}) for TIDs 1–3 using ray-differenced TEC. Panels (b), (e), and (h) show GNSS-MEO results, and panels (c), (f), and (i) show GEO-only results.

The clearest difference between the GEO and GNSS results is apparent in the ray-differenced TEC results. Unlike the GNSS case, the GEO inversion is essentially insensitive to the slowly changing background N_0, and therefore well suited to image MSTIDs which more often induce changes in TEC between sequential rays. It is also poorer in reconstructing the larger LSTIDs 1–3 for the same reason. These results indicate that the two satellite geometries are complementary. As the GEO rays are stationary, changes in TEC over 30 s caused by the temporal gradient in N_0 (IRI) are very small in comparison to the changes caused by a TID. Therefore, the GEO-only inversion essentially has no information on the TEC contribution from N_0, and solves only for the more rapid perturbations. For moving satellites, on the other hand, the change in TEC over 30 s is more substantial, as it is also affected by the spatial gradient in N_0.

3.6. Comparing LSTID and MSTID Results

The results show that the scale of the modeled TID has a large impact on the reconstruction results. The smallest TIDs (5–6) are especially difficult to reconstruct using GNSS-MEO geometry, with exaggerated amplitudes and noisy spatial artifacts in vTEC present in Figures 7 and 10. It is likely that these are caused by the distortion effects due to satellite motion detailed in section 1, which become prominent when the data time window of 1 hr is comparable to the TID wave period, and produces seemingly inconsistent TEC data. These distortions are not present in the GEO data, making it better suited for imaging MSTIDs.

At the other end of the spectrum, large LSTIDs are imaged slightly better using GNSS than GEO for precalibrated TEC inversions. This could be because GNSS simply has a higher number of visible satellites, and due to the limited viewing angles of the GEO satellites, which may introduce some latitudinal dependence in the wave amplitude. GNSS is also better for cases using ray-differenced TEC since the GEO ray-differenced inversion has difficulty detecting these large structures.

It is clear from Figures 5, 6, 9, and 8 that all inversions overestimate the peak height of the model. This is a result of the predefined Chapman profiles used to seed the EOFs, which provide the vertical structure for the inversion. These are the same for all inversions, and consequently, the *F* layer peak is consistently overestimated.

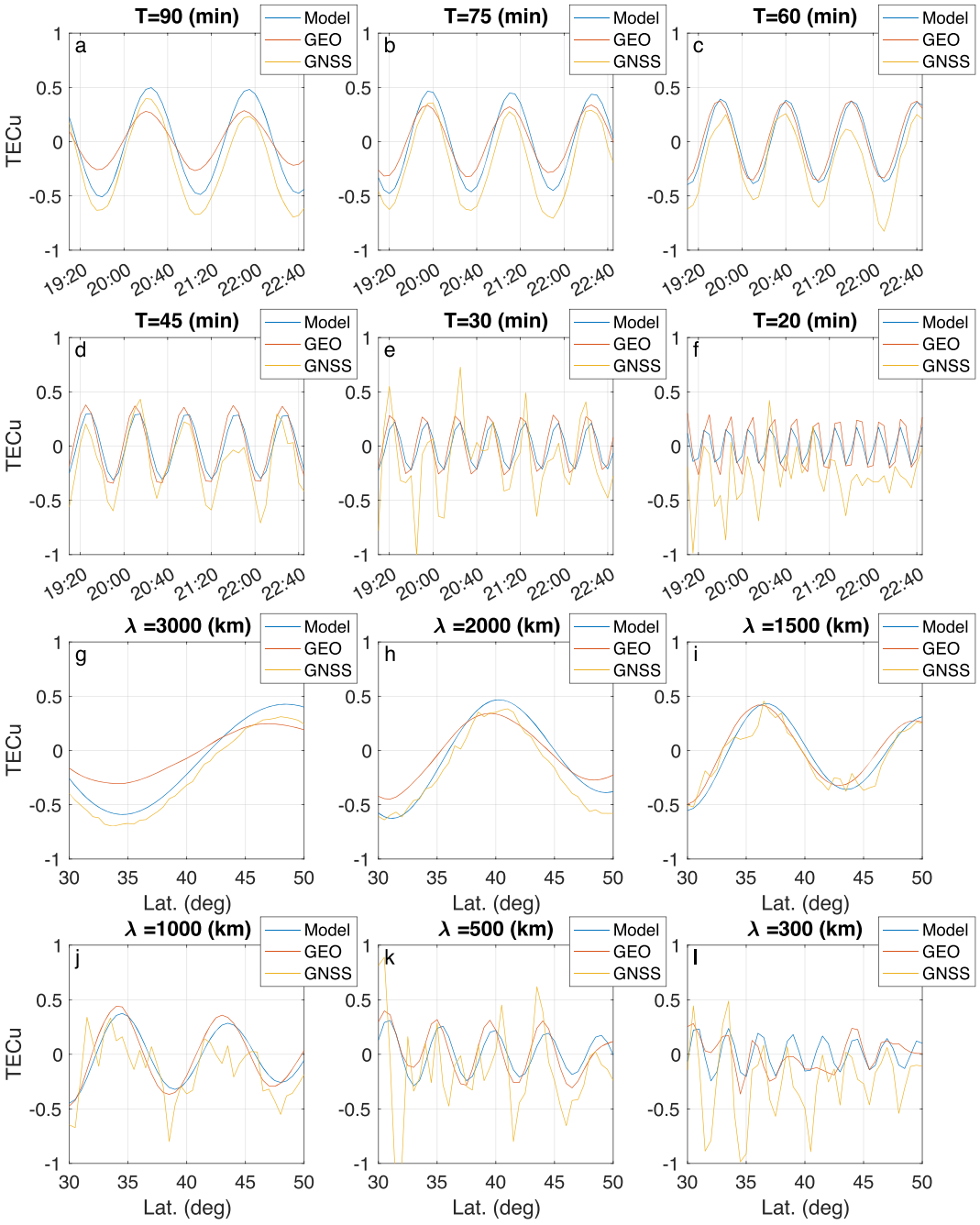

Figure 10. Ray-differenced inversion results ($vTEC_{\text{est}}^{\text{GNSS-MEO}} - vTEC_0$) and $vTEC_{\text{est}}^{\text{GEO}}$ plotted against the model δTEC.

3.7. Combining GEO and GNSS-MEO Geometry

Having now established that the two types of orbits have different effects on the resulting inversion, the next step is to examine the performance of both GEO and GNSS-MEO data together. The results in the above sections suggest that it could be beneficial to combine the GNSS and GEO in order to have a single method to more reliably detect TIDs of all scales. The simplest way to combine both satellite geometries is to use both the GEO and GNSS data sets simultaneously in one inversion without any weighting scheme.

The combined reconstruction is very similar to the GNSS-only reconstruction, as seen in Figure 11. A reason for this could be that there are generally more GNSS data available than GEO data, and that the moving GNSS rays can cover areas of the inversion grid that the stationary GEO rays do not, giving the GNSS data

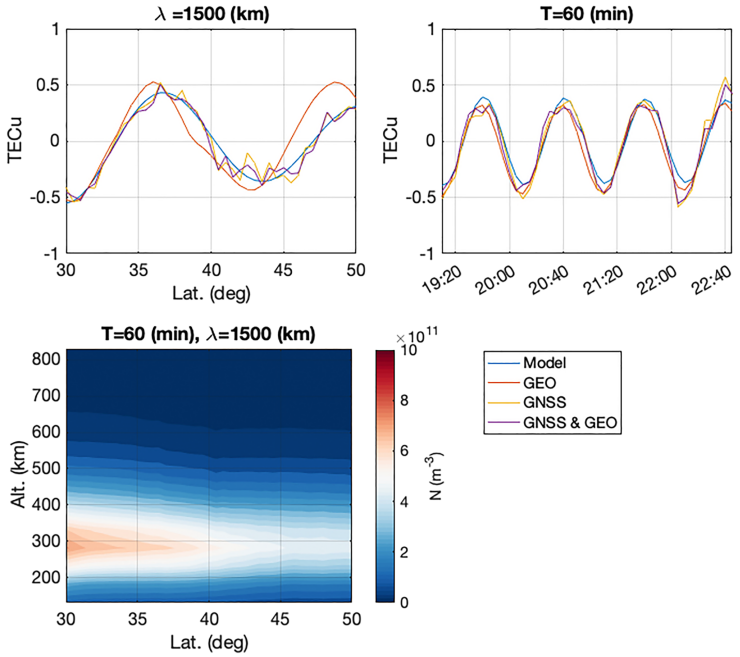

Figure 11. Inversion using precalibrated GEO and GNSS-MEO data combined for TID 3.

precedence. Essentially, the benefit of using the GEO signals is not realized when combined together with the GNSS data.

3.8. Summary of Section 3

The results of this section have shown that the MIDAS tomography algorithm is able to reconstruct TID-perturbed ionospheres using standard GNSS satellite geometry and GEO geometry. When used separately, there were distinct advantages seen with the different satellite geometries. Tables 2 and 3 summarize the results as root-mean-square errors (RMSEs) of vTEC sampled at a point in the center of the grid (40°N 98°W) for all sets of TID parameters in Table 1. Table 2 shows the RMSEs using precalibrated TEC, which are generally smaller than the errors from ray-differenced MIDAS results in Table 3. In general, both tables show an overall decreasing error with smaller TIDs for GEO-only results, and the opposite trend for GNSS-only and combined results. The combined results have equal or slightly lower RMSEs than the GNSS-only inversions for all but the two smallest TIDs, where the distortions from satellite movement are largest.

Table 2
Root-Mean-Square Errors (TECu) Between Estimated Vertical TEC Perturbation ($\delta vTEC_{est}$ for GEO,$\delta vTEC_{est} - vTEC_{IRI}$ for GNSS-MEO and combined) From Calibrated TEC Inversions and Perturbed vTEC of the input Model ($\delta vTEC_{sim}$)

Precalib.	TID_1	TID_2	TID_3	TID_4	TID_5	TID_6
T (min)	90	75	60	45	30	20
λ (km)	3,000	2,000	1,500	1,000	500	300
GEO	0.09	0.09	0.10	0.10	0.10	0.16
GNSS	0.04	0.06	0.10	0.15	0.27	0.18
Combined	0.03	0.06	0.09	0.15	0.26	0.21

Note. These correspond to panels (a)–(f) in Figure 7.

Table 3
Root-Mean-Square Errors (TECu) Between Estimated Vertical TEC Perturbation ($\delta vTEC_{est}$ for GEO,$\delta vTEC_{est} - vTEC_{IRI}$ for GNSS-MEO and Combined) From Ray-Differenced TEC Inversions and Perturbed vTEC of the Input Model ($\delta vTEC_{sim}$)

Ray-diff.	TID_1	TID_2	TID_3	TID_4	TID_5	TID_6
T (min)	90	75	60	45	30	20
λ (km)	3,000	2,000	1,500	1,000	500	300
GEO	0.18	0.12	0.07	0.10	0.10	0.13
GNSS	0.20	0.20	0.23	0.26	0.29	0.31
Combined	0.17	0.19	0.20	0.25	0.32	0.30

Note. These correspond to panels (a)–(f) in Figure 10.

4. Discussion and Conclusions

In this paper, we have used simulated TEC data sets to investigate the performance of the MIDAS ionospheric tomography algorithm in relation to TID imaging. These data sets are generated from different stationary and moving satellite geometries through modeled TIDs. The results suggest that GNSS-MEO satellite geometry is preferred for LSTIDs with wave periods above 1 hr. GEO geometry performs better for medium-scale TIDs.

For GNSS-MEO, there is a clear effect of satellite movement introducing distortions of the TID perturbed TEC, as shown by Wan et al. (1997), and this can have a subsequent effect on the tomographic images produced by MIDAS by distorting the input TEC data. This effect appears to be most prominent for MSTIDs.

When using MIDAS in ray-differenced mode with GEO TEC, the TID structures are reproduced separated from the background ionosphere, even for medium-scale TIDs. Using MIDAS in precalibrated mode with GEO TEC produced full inversions including the background ionosphere and showed improvement over GNSS-only TEC for MSTIDs.

This study did not find that inversion using a direct combination of both GNSS and GEO data offered any major advantages when imaging TIDs. A possible future development of the reconstruction method could use a weighting scheme giving GEO observations precedence during the inversion. This could improve imaging of MSTIDs, while still making use of the full GNSS geometry.

An inherent difference between the GEO and GNSS geometries is the limited viewing angle of a GEO satellite, all of which are positioned over the equator. If the geometry is such that the ray does not cut through the trough and crest of the wave, it can even be the case that the ray intersects two or more wavefronts. In this case an increase in density where the ray intersects one wavefront is compensated for by a depletion where the ray intersects another wavefront. This is described as the *phase cancelation effect* by Georges and Hooke (1970). For this reason, there are only a certain range of latitudes where the viewing geometry from a ground-based receiver will be favorable for GEO TID observations.

This study used purely simulated observations from a modeled ionosphere. It still remains to apply these methods on real data known to contain TIDs and to verify against independent observations. When using real GNSS signal observations, there are several considerations to be taken into account. First, the real ionosphere will of course differ from the models used here, and will often be much more dynamic, and not as well behaved. For example, in addition to TIDs there may be other large-scale perturbations present that could obscure the TID signatures. There may also be several TIDs present at once, and the method presented here does not include a strategy for separating them out. The Hooke TID model used here considers TIDs as relative perturbations, so the wave amplitudes scale with the local level of ionization. This means that for these results, a stronger or weaker ionosphere would not make the TIDs more or less difficult to image. In a real case however, a weaker ionosphere makes the TID TEC perturbations smaller in absolute terms, and so are more difficult to discern in the presence of noise. Second, if using uncalibrated real TEC with MIDAS, the MIDAS calibration accuracy can be expected at around 1 TECu (Dear, 2007) and could thus limit reliable detection of TIDs to those with amplitudes larger than 1 TECu. Achieving GNSS IFB calibration to a level better than 1 TECu is challenging, as equipment limitations (temperature variations) are fundamental to the calibration and would have to be modeled into the process to increase the accuracy of the instantaneous

IFB estimation. Finally, the number and type of geostationary navigation satellites in view varies geographically. Here, it is assumed that all GNSS receivers receive the signals from three SBAS GEO satellites. In practice some SBAS satellites transmit only one frequency, thus requiring an additional step of processing as described by Cooper et al. (2019). Geostationary satellites that broadcast a full GNSS signal, such as Beidou GEO satellites, can be used for direct TEC measurements (Kunitsyn et al., 2016) in areas where they provide coverage.

The methods presented in this paper can be applied to GNSS observations over different regions of the world to investigate the spatial and temporal characteristics of TIDs from a statistical viewpoint. These can then be related to proposed mechanisms of TID generation to uncover which mechanisms are prevalent for different TID observations and classes. Interesting outstanding questions about TIDs include the source mechanisms such as thunderstorms and other meteorological disturbances (Azeem & Barlage, 2018), geomagnetic storms, and auroral energy deposition. Other more unusual anthropogenic causes could also be considered, such as those investigated by Scott and Major (2018). These types of investigations require TID tracking over large areas to infer not only the spatial and temporal wave characteristics locally, but also the TID direction and hence the source region. The potential to use distributed GNSS and GEO observations for these types of ionospheric studies is very promising.

Taking into account the challenges that still remain, The geostationary orbit offers a unique vantage point for observing traveling ionospheric disturbances, where the motion of the satellite does not produce frequency shifts to oscillations in TEC. and will provide a valuable input into ionospheric tomography and data assimilation algorithms concerned with TID imaging in the future.

Acknowledgments
The GNSS orbits used in this study were provided by the International GNSS Service (http://www.igs.org/). The authors acknowledge funding by Horizon 2020 Marie Skłodowska-Curie Actions Grant Agreement 722023 and NERC Fellowship NE/P006450/1.

References

Andreeva, E., Kunitsyn, V., & D. Tereshchenko, E. (1992). Phase difference radio tomography of the ionosphere. *Geomagnetism and Aeronomy/Geomagnetizm i Aeronomiia*, *32*, 104–110.

Austen, J. R., Franke, S. J., & Liu, C. H. (1988). Ionospheric imaging using computerized tomography. *Radio Science*, *23*(3), 299–307. https://doi.org/10.1029/RS023i003p00299

Azeem, I., & Barlage, M. (2018). Atmosphere-ionosphere coupling from convectively generated gravity waves. *Advances in Space Research*, *61*(7), 1931–1941. https://doi.org/10.1016/j.asr.2017.09.029

Bilitza, D., Altadill, D., Truhlik, V., Shubin, V., Galkin, I., Reinisch, B., & Huang, X. (2017). International reference ionosphere 2016: From ionospheric climate to real-time weather predictions. *Space Weather*, *15*, 418–429. https://doi.org/10.1002/2016SW001593

Bruno, J., Mitchell, C. N., Bolmgren, KarlHA, & Witvliet, B. A. (2020). A realistic simulation framework to evaluate ionospheric tomography. *Advances in Space Research*, *65*(3), 891–901. https://doi.org/10.1016/j.asr.2019.11.015

Bust, G. S., & Mitchell, C. N. (2008). History, current state, and future directions of ionospheric imaging. *Reviews of Geophysics*, *46*, RG1003. https://doi.org/10.1029/2006RG000212

Cervera, M. A., & Harris, T. J. (2014). Modeling ionospheric disturbance features in quasi-vertically incident ionograms using 3-D magnetoionic ray tracing and atmospheric gravity waves. *Journal of Geophysical Research: Space Physics*, *119*, 431–440. https://doi.org/10.1002/2013JA019247

Chapman, S. (1931). The absorption and dissociative or ionizing effect of monochromatic radiation in an atmosphere on a rotating earth. In *Proceedings of the Physical Society* (pp. 26–45).

Chen, C. H., Saito, A., Lin, C. H., Yamamoto, M., Suzuki, S., & Seemala, G. K. (2016). Medium-scale traveling ionospheric disturbances by three-dimensional ionospheric GPS tomography 3. Space science. *Earth, Planets and Space*, *68*(1), 32. https://doi.org/10.1186/s40623-016-0412-6

Cook, J. A., & Close, S. (1995). An investigation of TID evolution observed in MACE'93 data. *Annals of Geophysics*, *13*, 1320–1324.

Cooper, C., Mitchell, C. N., Wright, C. J., Jackson, D. R., & Witvliet, B. A. (2019). Measurement of ionospheric total electron content using single-frequency geostationary satellite observations. *Radio Science*, *54*, 10–19. https://doi.org/10.1029/2018RS006575

Davis, M. J., & da Rosa, A. V. (1969). Traveling ionospheric disturbances originating in the auroral oval during polar substorms. *Journal of Geophysical Research*, *74*(24), 5721–5735. https://doi.org/10.1029/JA074i024p05721

Dear, R. M. (2007). Wide-area forecasting of total electron content over Europe (Doctoral Dissertation), University of Bath.

Dear, R. M., & Mitchell, C. N. (2006). GPS interfrequency biases and total electron content errors in ionospheric imaging over Europe. *Radio Science*, *41*, RS6007. https://doi.org/10.1029/2005RS003269

Georges, T. M., & Hooke, W. H. (1970). Wave-induced fluctuations in ionospheric electron content: A model indicating some observational biases. *Journal of Geophysical Research*, *75*(31), 6295–6308. https://doi.org/10.1029/JA075i031p06295

Hernández-Pajares, M., Juan, J. M., & Sanz, J. (2006a). Real time MSTIDs modelling and application to improve the precise GPS and GALILEO navigation, *Proceedings of the 19th International Technical Meeting of the Satellite Division of the Institute of Navigation (Ion GNSS 2006)* (pp. 1358–1368). Fort Worth, TX.

Hernández-Pajares, M., Juan, J. M., & Sanz, J. (2006b). Medium-scale traveling ionospheric disturbances affecting GPS measurements: Spatial and temporal analysis. *Journal of Geophysical Research*, *111*, A07S11. https://doi.org/10.1029/2005JA011474

Hines, C. O. (1960). Internal amospheric gravity waves at ionospheric heights. *Canadian Journal of Physics*, *38*(11), 1441–1481. https://doi.org/doi/10.1139/p60-150

Hocke, K., & Schlegel, K. (1996). A review of atmospheric gravity waves and travelling ionospheric disturbances: 1982-1995. *Annales Geophysicae*, *14*(9), 917–940. https://doi.org/10.1007/s00585-996-0917-6

Hooke, W. H. (1968). Ionospheric irregularities produced by internal atmospheric gravity waves. *Journal of Atmospheric and Terrestrial Physics*, *30*(5), 795–823. https://doi.org/10.1016/S0021-9169(68)80033-9

Huang, F., Lei, J., Dou, X., Luan, X., & Zhong, J. (2018). Nighttime medium-scale traveling ionospheric disturbances from airglow imager and global navigation satellite systems observations. *Geophysical Research Letters*, *45*, 31–38. https://doi.org/10.1002/2017GL076408

Kunitake, M., Ohtaka, K., Maruyama, T., Tokumaru, M., Morioka, A., & Watanabe, S. (1995). Tomographic imaging of the ionosphere over Japan by the modified truncated SVD method. *Annales Geophysicae*, *13*, 1303–1310.

Kunitsyn, V. E., Padokhin, A. M., Kurbatov, G. A., Yasyukevich, Y. V., & Morozov, Y. V. (2016). Ionospheric TEC estimation with the signals of various geostationary navigational satellites. *GPS Solutions*, *20*(4), 877–884. https://doi.org/10.1007/s10291-015-0500-2

Lee, J. K., Kamalabadi, F., & Makela, J. J. (2008). Three-dimensional tomography of ionospheric variability using a dense GPS receiver array. *Radio Science*, *43*, RS3001. https://doi.org/10.1029/2007RS003716

Mitchell, C. N., Rankov, N. R., Bust, G. S., Miller, E., Gaussiran, T., Calfas, R., et al. (2017). Ionospheric data assimilation applied to HF geolocation in the presence of traveling ionospheric disturbances. *Radio Science*, *52*, 829–840. https://doi.org/10.1002/2016RS006187

Mitchell, C. N., & Spencer, P. S. J. (2003). A three-dimensional time-dependent algorithm for ionospheric imaging using GPS. *Annals of Geophysics*, *46*(4), 687–696. https://doi.org/10.4401/ag-4373

Morgan, M. G., & Calderón, C. H. J. (1978). Testing Hooke's perturbation formula for the production of TID's by gravity waves. *Journal of Geophysical Research*, *83*(A12), 5737–5740.

Munro, G. H. (1950). Travelling disturbances in the ionosphere. *Proceedings of the Royal Society of London. Series A, Mathematical and Physical Sciences*, *202*, 208–223. https://doi.org/10.1098/rspa.1950.0095

Nickisch, L. J., Fridman, S., Hausman, M., & San Antonio, G. S. (2016). Feasibility study for reconstructing the spatial-temporal structure of TIDs from high-resolution backscatter ionograms. *Radio Science*, *51*, 443–453. https://doi.org/10.1002/2015RS005906

Nygrén, T, Aikio, A. T., Voiculescu, M., & Cai, L. (2015). Radar observations of simultaneous traveling ionospheric disturbances and atmospheric gravity waves. *Journal of Geophysical Research: Space Physics*, *120*, 3949–3960. https://doi.org/10.1002/2014JA020794

Penney, R. W., & Jackson-Booth, N. K. (2015). Mitigating satellite motion in GPS monitoring of traveling ionospheric disturbances. *Radio Science*, *50*, 1150–1164. https://doi.org/10.1002/2015RS005767

Pryse, S. E., Mitchell, C. N., Heaton, J. A. T., & Kersley, L. (1995). Travelling ionospheric disturbances imaged by tomographic techniques. *Annales Geophysicae*, *13*(12), 1325–1330.

Saito, A., Fukao, S., & Miyazaki, S. (1998). High resolution mapping of TEC perturbations with the GSI GPS network over Japan. *Geophysical Research Letters*, *25*(16), 3079–3082. https://doi.org/10.1029/98GL52361

Scott, C. J., & Major, P. (2018). The ionospheric response over the UK to major bombing raids during World War II. *Annales Geophysicae*, *36*(5), 1243–1254. https://doi.org/10.5194/angeo-36-1243-2018

Ssessanga, N., Kim, Y. H., & Kim, E. (2015). Vertical structure of medium-scale traveling ionospheric disturbances. *Geophysical Research Letters*, *42*, 9156–9165. https://doi.org/10.1002/2015GL066093

Tang, J., Yao, Y., Kong, J., & Zhang, L. (2016). Large-scale traveling ionospheric disturbances using ionospheric imaging at storm time: A case study on 17 March 2013. *Journal of Atmospheric and Solar: Terrestrial Physics*, *145*, 12–20. https://doi.org/10.1016/j.jastp.2016.04.006

Thébault, E., Finlay, C. C., Beggan, C. D., Alken, P., Aubert, J., Barrois, O., et al. (2015). International geomagnetic reference field: The 12th generation. *Earth, Planets and Space*, *67*(1), 79. https://doi.org/10.1186/s40623-015-0228-9

Van De Kamp, M., Pokhotelov, D., & Kauristie, K. (2014). TID characterised using joint effort of incoherent scatter radar and GPS. *Annales Geophysicae*, *32*(12), 1511–1532. https://doi.org/10.5194/angeo-32-1511-2014

Wan, W., Ning, B., Yuan, H., Li, J., & Li, L. (1997). TID observation using a short baseline network of GPS receivers. *Acta Geodaetica et Geophysica Hungarica*, *32*(3-4), 321–327.

Yin, P., Zheng, Y. N., Mitchell, C. N., & Li, B. (2017). A multiresolution inversion for imaging the ionosphere. *Journal of Geophysical Research: Space Physics*, *122*, 6799–6811. https://doi.org/10.1002/2016JA023728

Yizengaw, E., Dyson, P. L., Essex, E. A., & Moldwin, M. B. (2005). Ionosphere dynamics over the Southern Hemisphere during the 31 March 2001 severe magnetic storm using multi-instrument measurement data. *Annales Geophysicae*, *23*(3), 707–721. https://doi.org/10.5194/angeo-23-707-2005